Ceramics International xxx (xxxx) xxx

Contents lists available at ScienceDirect

Ceramics International

journal homepage: www.elsevier.com/locate/ceramint

Enhanced high-temperature oxidation resistance of compositionally optimized medium-entropy carbide $(Hf_{1/3}Ta_{1/3}Ti_{1/3})C$

Guoming Yi [a,b], Juan Kuang [a,b], Gaopeng Zou [a,b], Bo Sun [a,b], Huanyu Mo [a,b], Qianqian Wang [a,b,c,*], Baolong Shen [a,b,**]

[a] School of Materials Science and Engineering, Jiangsu Key Laboratory for Advanced Metallic Materials, Southeast University, Nanjing, 211189, China
[b] Ministry of Education Key Laboratory of Structure and Thermal Protection for High-Speed Aircraft, Southeast University, Nanjing, 211189, China
[c] Jiangsu Key Laboratory of Advanced Structural Materials and Application Technology, Nanjing Institute of Technology, Nanjing, 211167, China

ARTICLE INFO

Keywords:
High-temperature oxidation
High-entropy carbides
Medium-entropy carbides
Preferential oxidation
HfTa-Based ceramics

ABSTRACT

Excellent oxidation resistance is crucial for ultra-high temperature ceramics in extreme service environments. The oxidation behavior and mechanism of $(Hf_{1/3}Ta_{1/3}Zr_{1/3})C$, $(Hf_{1/3}Ta_{1/3}Nb_{1/3})C$, $(Hf_{1/3}Ta_{1/3}Ti_{1/3})C$ and $(Hf_{0.2}Ta_{0.2}Ti_{0.2}Zr_{0.2}Nb_{0.2})C$ prepared by spark plasma sintering were investigated. The Zr and Nb/Ta oxides can lead to the powdering and cracking of the oxide layer in $(Hf_{1/3}Ta_{1/3}Zr_{1/3})C$ and $(Hf_{1/3}Ta_{1/3}Nb_{1/3})C$ during oxidation. The sluggish diffusion effect and synergistic effect of multi-principal elements enable $(Hf_{0.2}Ta_{0.2}Ti_{0.2}Zr_{0.2}Nb_{0.2})C$ to form a denser and thinner oxide layer at 1300 °C. The alternating dense/porous layered oxide of $(Hf_{1/3}Ta_{1/3}Ti_{1/3})C$ formed at 1450 °C and 1500 °C functions as an oxygen diffusion barrier and thermal stress management. The similar oxidation rate of Hf, Ta, and Ti weakens the preferential oxidation tendency, and thus maintains the stability of the configurational entropy of the $(Hf_{1/3}Ta_{1/3}Ti_{1/3})C$. The oxidation resistance of the $(Hf_{0.2}Ta_{0.2}Ti_{0.2}Zr_{0.2}Nb_{0.2})C$ deteriorates significantly at 1450 °C, and fails at 1500 °C due to the loss of low-melting-point oxides and excessive thermal stress. This work demonstrates the temperature-dependent effectiveness of high-entropy design strategies and provides foundational insights for tailoring UHTCs across distinct temperature regimes.

1. Introduction

Developing thermal protection systems with exceptional durability is imperative for critical high-temperature applications, e.g., the leading edge of hypersonic vehicles, rocket propulsion components, and advanced energy conversion systems under severe thermal loads [1–5]. Ultra-high temperature ceramics (UHTCs), including carbides, nitrides, and borides of early transition metals, exhibit high melting points exceeding 3000 °C, high hardness, and outstanding thermal/chemical stability, making them promising candidates at elevated temperatures [6–10]. Among the UHTCs, HfC and TaC show extremely high melting points (>3800 °C), which offer them great potential for application in aerospace thermal protection materials (TPMs) [11–13]. Their identical NaCl-type crystal structure (B1-type, Fm3m space group) enables the formation of continuous HfTa-based solid solutions [6,14], thus leading to the advancement of their physical and chemical properties [15–18]. However, the oxidation resistance of HfTa-based ceramics remains insufficient for complex high-temperature oxidizing environments, necessitating further optimization.

Superior oxidation resistance is a fundamental requirement for materials to maintain structural integrity while preserving their exceptionally high-temperature mechanical properties [19]. It has been evidenced that the multicomponent design strategy can effectively improve the oxidation resistance of single-component UHTCs [18, 20–22]. Formation of complex oxide phases may enhance the oxidation resistance, offering a key benefit of high-entropy materials compared to traditional alloys and ceramics [23,24]. Newly developed high-entropy and medium-entropy carbides (HECs and MECs), including (NbTaZrHfTi)C [25–28], (ZrNbHfTa)C [29–31], and (ZrHfTi)C [32–34] have shown enhanced oxidation resistance at different temperatures.

* Corresponding author. School of Materials Science and Engineering, Jiangsu Key Laboratory for Advanced Metallic Materials, Southeast University, Nanjing, 211189, China.
** Corresponding author. School of Materials Science and Engineering, Jiangsu Key Laboratory for Advanced Metallic Materials, Southeast University, Nanjing, 211189, China.
E-mail addresses: qwang678@seu.edu.cn (Q. Wang), blshen@seu.edu.cn (B. Shen).

https://doi.org/10.1016/j.ceramint.2026.01.115
Received 21 October 2025; Received in revised form 25 December 2025; Accepted 8 January 2026
Available online 9 January 2026

Due to the increased entropy of these carbides, a complex and high-melting-point oxide layer with dense microstructure can be formed during the oxidation, which contributes significantly to the enhanced stability by impeding oxygen diffusion into the bulk material.

The oxidation resistance of UHTCs is fundamentally governed by not only the entropy but also the elemental composition. The constituent elements are the foundational determinant of baseline oxidation resistance performance [19]. Adding transition metal elements into the cation sublattice can increase configurational entropy. However, the incorporation of specific elements may substantially compromise oxidation resistance. Chen et al. [35] systematically investigated the oxidation behavior of (NbTaZrW)C at 800–1000 °C, revealing that the presence of W resulted in significantly higher parabolic rate constants (k_p) and thicker oxide layers compared to (HfZrTaNbTi)C and (HfTaZrNb)C. Due to the low melting point of corresponding oxides, the oxidation behavior of W, Mo, and V was dominated by gaseous oxide species, which resulted in porosity in the oxide layer [36]. Additionally, the formation of ZrO_2 in ZrC ceramics usually introduces internal stresses within the oxide layer during temperature cycling, resulting in volume expansion and cracks [37,38]. These previous studies have confirmed the significant improvement in oxidation resistance achieved through multi-component design strategies, while the selection of constituent components played an equally critical role in determining oxidation resistance.

In this study, medium-entropy carbides including $(Hf_{1/3}Ta_{1/3}Zr_{1/3})C$, $(Hf_{1/3}Ta_{1/3}Nb_{1/3})C$, and $(Hf_{1/3}Ta_{1/3}Ti_{1/3})C$, as well as high-entropy carbide $(Hf_{0.2}Ta_{0.2}Ti_{0.2}Zr_{0.2}Nb_{0.2})C$, denoted as HTZ, HTN, HTT, and HTTZN, respectively, were synthesized via spark plasma sintering (SPS). This study aims to delineate the distinct roles of constituent elements in oxidation at elevated temperatures, while concurrently exploring the entropy-driven stabilization effects within the oxide layer evolution, which provides critical insights for the rational design and performance optimization of UHTCs through entropy-composition engineering.

2. Experimental

2.1. Sample preparation

The commercial carbide powders of HfC, TaC, ZrC, NbC, and TiC (purity>99.9 %, 1–3 μm, D 50 value) were purchased from QinBang Co., Ltd (Hebei, China). The equiatomic mixture of carbide powder was put into a tungsten carbide jar and ball milled in ethanol solution at 300 rpm for 8 h. The milling process was paused every 20 min for 10 min to prevent overheating of mixed powders. The slurry was dried at 80 °C for 12 h in a vacuum oven and sieved through a 200-mesh stainless steel sieve. The prepared powder was consolidated via spark plasma sintering (SPS, LABOX-325R, Japan) under a uniaxial pressure of 50 MPa, with a heating rate of 100 °C/min to 2000 °C, followed by 45 min isothermal sintering. The relative density of the sintered specimens was measured via the Archimedes method.

2.2. Oxidation test

Specimens with dimensions of 6 mm × 6 mm × 3 mm were extracted from the sintered bulk by wire-cutting, and then polished using SiC papers sequentially up to 2000 grit. Isothermal oxidation tests were conducted at 1300–1500 °C in a muffle furnace in air. After reaching the target temperature, the specimens were immediately put into the furnace, and mass changes were recorded at 20-min intervals. Three independent measurements were performed for each specimen, and the average value was used to ensure data reliability. To determine whether the oxidation behavior follows a parabolic rate law, the data were fitted using the following equation [30]:

$$(\Delta W/A)^2 = k_p t \quad (1)$$

where ΔW is the mass change (mg), A is the area (cm^2), k_p is the parabolic oxidation rate constant, and t is the time (min). To investigate the effects of thermal cycling on the oxide layer, continuous static oxidation tests were conducted without taking out for weighing.

2.3. Structure characterization

The phases of the specimens were characterized by X-ray diffraction (XRD) with Cu Kα (Rigaku D/max2500, Japan). The surface and cross-section morphology of the oxide layer was characterized by scanning electron microscopy (SEM, FEI Sirion 200, USA) with energy dispersive spectrometry (EDS). The average grain size was measured using the linear intercept method. The grain size is quantified by overlaying straight lines on a SEM image and counting the number of intersections with grain boundaries. The crystal structure of the oxide was characterized using a high-resolution transmission electron microscope (HRTEM, Talos F200X, USA). The TEM specimens were prepared from ground powder obtained from the oxide layer.

3. Results and discussion

3.1. Microstructure of as-sintered medium/high-entropy carbides

The XRD patterns of the as-sintered medium/high-entropy carbides are presented in Fig. 1(a). All specimens exhibit exclusively five characteristic diffraction peaks corresponding to a single solid-solution carbide phase with the space group of *Fm3m*, confirming the successful synthesis of single-phase materials. Compared to the diffraction peaks of HTZ, the diffraction peaks of HTT and HTN exhibited distinct rightward shifts to higher angles, which can be attributed to variations in atomic radii among constituent elements. Rietveld refinement of the XRD patterns yielded lattice parameters of 4.5824, 4.5169, 4.4809, and 4.5211 Å for HTZ, HTN, HTT, and HTTZN, respectively. Representative crystal structure of the medium/high-entropy carbides is shown in Fig. 1(b), showing a rock-salt structure.

Fig. 2 displays the surface morphology and corresponding EDS analyses of four as-sintered ceramic specimens. The EDS mapping results show a homogeneous distribution of transition metal elements across all specimens. However, segregation of Hf was observed in the HTN specimen from the SEM image and the corresponding EDS mapping in Fig. 2 (b), which is also observed in the previous finding [39]. The oxygen content in all specimens remained below the detection limit of EDS mapping analysis, demonstrating effective control of raw material oxidation during both powder preparation and sintering processes. The relative densities of all specimens ranged from 94 % to 97 %, which is close enough not to significantly influence the oxidation process.

3.2. Optimization of the MECs

Group IV, V, and VI transition metals (Hf, Nb, Ta, Ti, and Zr) have garnered significant attention in ultra-high temperature applications due to the exceptionally high melting points of their respective carbides and oxides (Fig. S1). For preliminary screening of oxidation-resistant Hf-Ta medium-entropy carbide ceramics (MECCs), 3 representative MEC systems (HTZ, HTN, and HTT) were designed for preliminary oxidation resistance evaluation. The mass gain curves obtained at 1300 °C and 1400 °C are presented in Fig. S2. HTN demonstrates the highest mass gain at both temperatures, while the record of mass gain of HTZ stopped at 20 min due to catastrophic disintegration of the bulk specimen into fine fragments. The macroscopic view and surface morphology of the HTZ, HTN, and HTT after oxidation at 1400 °C for 2 h are shown in Fig. 3. As shown in Fig. 3(a) and the insert image, the HTZ specimen exhibited complete structural disintegration after oxidation. This is because phase transformation from t-ZrO_2 to monoclinic ZrO_2 (m-ZrO_2) occurred during heating and cooling, which lead to the volume

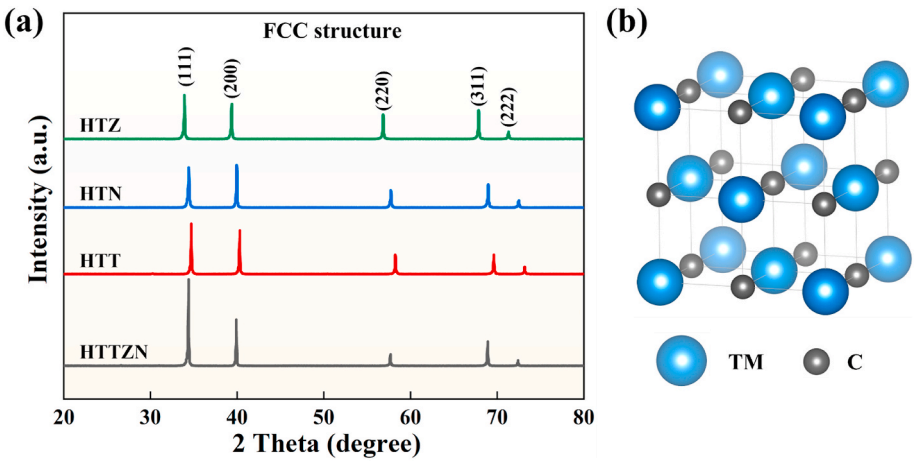

Fig. 1. (a) XRD patterns of the bulk ceramics prepared through SPS; (b) Crystal structure of medium/high-entropy carbides (Rock-salt), TM stands for transition metal atom, C stands for carbon atom.

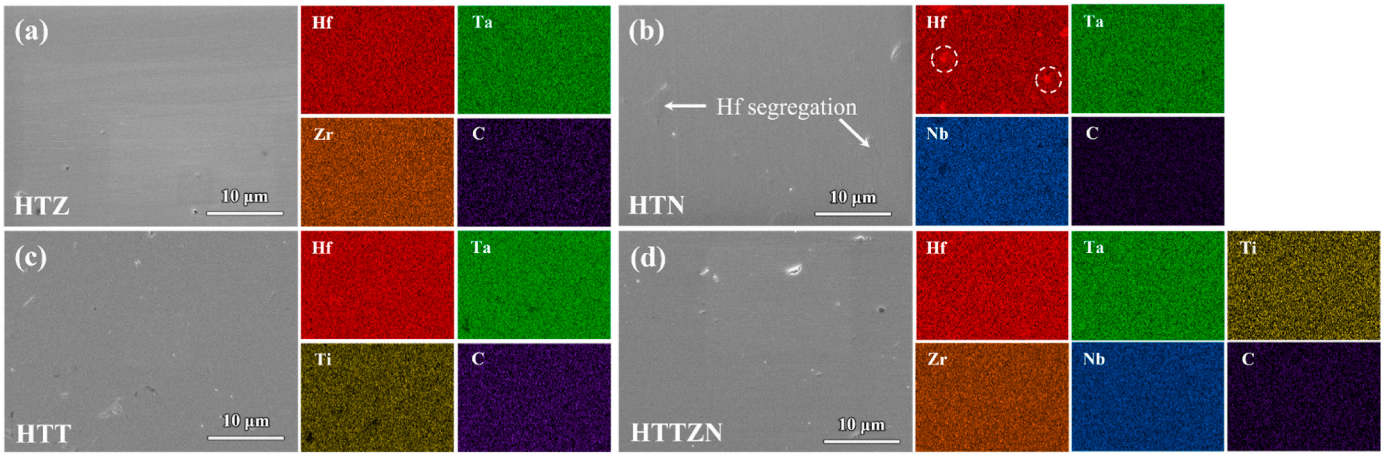

Fig. 2. SEM images and EDS analyses of the as-sintered (a) HTZ; (b) HTN; (c) HTT; and (d) HTTZN.

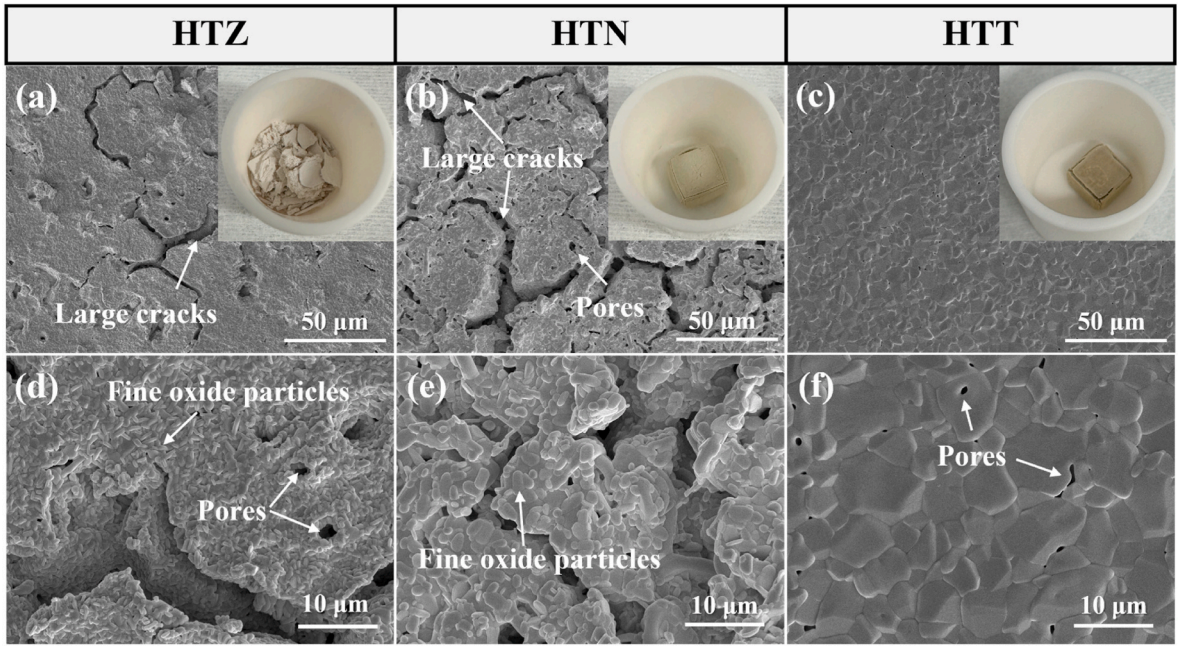

Fig. 3. SEM images and macroscopic morphology after oxidation at 1400 °C for 2 h. (a) and (d) HTZ; (b) and (e) HTN; (c) and (f) HTT.

expansion [37,40]. For HTN, extensive large cracks and pores were observed in Fig. 3(b) and (e), which can be attributed to volume expansion during oxidation originating from the high Pilling-Bedworth ratio (PBR, $V_{oxide}/V_{carbide}$) value of Nb/Ta oxides. (Corresponding XRD patterns are shown in Fig. S3 and the PBR value of $(TaNb)_2O_5$ is about 2.45 [19]) In contrast, a remarkably dense and continuous oxide layer formed on HTT after oxidation, as evidenced in Fig. 3(c). Only a limited number of small pores were observed on the surface in Fig. 3(f). Owing to the notably inferior oxidation resistance exhibited by both HTN and HTZ within the 1300–1400 °C range, further tests at elevated temperatures were deemed unnecessary. Subsequent investigations focused on conducting a systematic comparative analysis between the high-performance HTT and the extensively studied high-entropy carbide ceramic HTTZN, aiming to comprehensively evaluate the oxidation resistance of HTT.

3.3. Oxidation behavior of HTT and HTTZN

To investigate the oxidation behavior, comparative isothermal oxidation tests were conducted on HTT and HTTZN specimens at 1300 °C, 1400 °C, 1450 °C, and 1500 °C for 2 h, with the macroscopic pictures shown in Fig. 4. At 1300 °C and 1400 °C, the oxide layer of HTT and HTTZN both remained compact without spallation, while the cracks in the HTT corners were more evident than those of HTTZN. The surface morphology of the HTT and HTTZN began to show significant differences at 1450 °C. Few cracks were observed on the surface of HTT at 1450 °C, while the oxide layer on the HTTZN surface started to delaminate, exhibiting observable warping and large cracks. At 1500 °C, the HTT specimen retained its original block morphology with minor cracks and spallation. However, the oxide layer on HTTZN underwent severe deformation accompanied by catastrophic cracking at 1500 °C, ultimately leading to complete oxidation failure. The results indicated that 1450 °C served as a critical threshold temperature, beyond which HTT exhibited a remarkable reversal in oxidation resistance compared to HTTZN.

Fig. 5 presents the mass gain ($\Delta W/A$) and square of specific mass change $(\Delta W/A)^2$ as a function of oxidation time at 1300–1500 °C obtained from isothermal oxidation tests for HTT and HTTZN. As shown in Fig. 5(a) and (b), during the first 20 min of oxidation at each temperature, both HTT and HTTZN exhibited rapid mass gain due to the fast formation of the oxide layer. The HTTZN exhibited slower mass gain at 1300 °C and 1400 °C. Both HTT and HTTZN obeyed the parabolic law, which was controlled by a rate-limiting diffusion process. However, the mass gain of HTTZN exceeded that of HTT at 1450 °C, and a significant increase in mass gain was observed at 1500 °C. Although HTT demonstrates slightly higher mass gain at 1300 °C and 1400 °C, its mass gain maintained a stable and relatively low level at elevated temperatures (1450 °C and 1500 °C). For HTTZN, after 80 min of oxidation at 1500 °C, the mass gain stabilized with minimal variation, indicating that the substrate was completely oxidized and the oxide layer failed.

Table 1 lists the parabolic rate constant (k_p) and oxidation activation energy values of HTT and HTTZN at different temperatures obtained from Fig. 5(c) and (d). The relationship between the oxidation rate and temperature follows the Arrhenius-type formula shown in Eq. (2) [41] as follows:

$$k_p = k_0 \exp(-E/RT) \tag{2}$$

where k_0 denotes a pre-exponential constant, E represents the apparent oxidation activation energy, R is the gas constant, and T is the oxidation temperature, respectively. The activation energy was determined through linear regression analysis of the ln k_p versus $1000/T$ plots. At 1300 °C and 1400 °C, the k_p of HTTZN was lower than that of HTT, indicating a lower oxidation rate. As the temperature reached 1450 °C, the k_p of HTTZN increased to three times that of HTT, which is consistent with the mass gain trend in Fig. 5(a) and (b). The oxidation activation energy of HTTZN, calculated from 1300 °C to 1450 °C (parabolic law period), was 434.27 kJ/mol, which was significantly higher than that of HTT (185.36 kJ/mol), suggesting an elevated energy barrier during oxidation for HTTZN. This can be attributed to the sluggish diffusion effect induced by high-entropy characteristics, which significantly impeded the diffusion kinetics of oxygen atoms during the oxidation [42]. At 1500 °C, the oxidation rate of HTT increased steadily and slowly with the increase of temperature, indicating its outstanding oxidation resistance. However, HTTZN experienced a complete oxidation failure at 1500 °C, and the oxidation kinetics deviated from the parabolic rate law, rendering the oxidation rate undeterminable.

Fig. 6 presents the mass gain of different medium and high-entropy carbides after 2 h oxidation at varied temperatures. The performance varied significantly among the systems due to the compositional difference. HTTZN consistently showed minimal mass gain in both

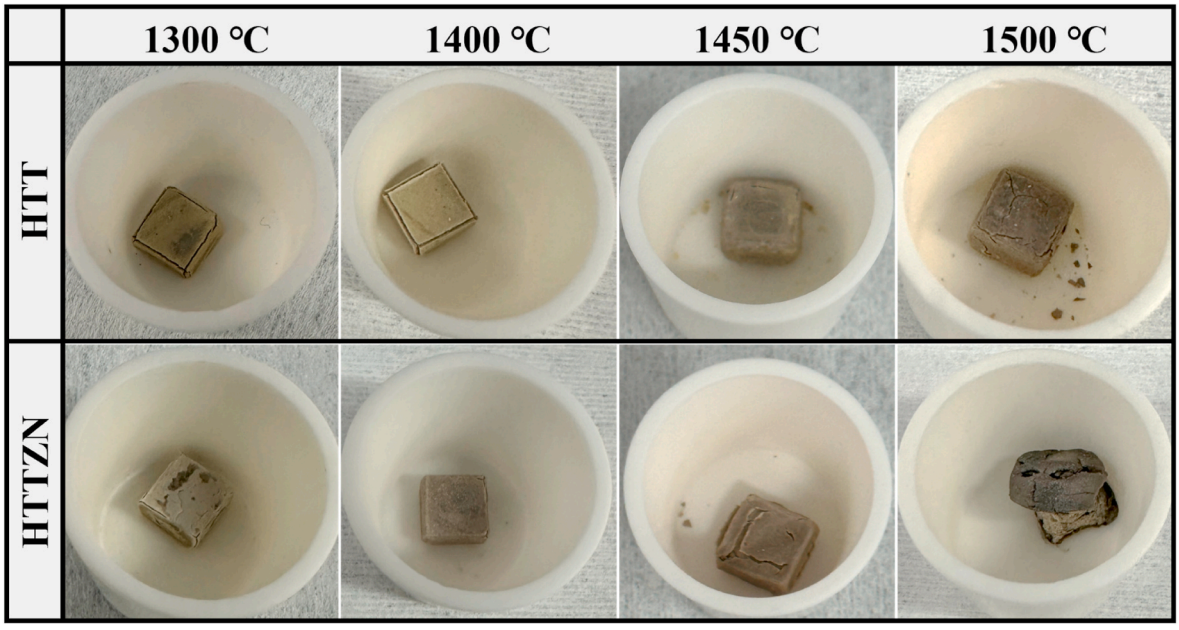

Fig. 4. Macroscopic morphology of HTT and HTTZN after oxidation at 1300–1500 °C for 2 h.

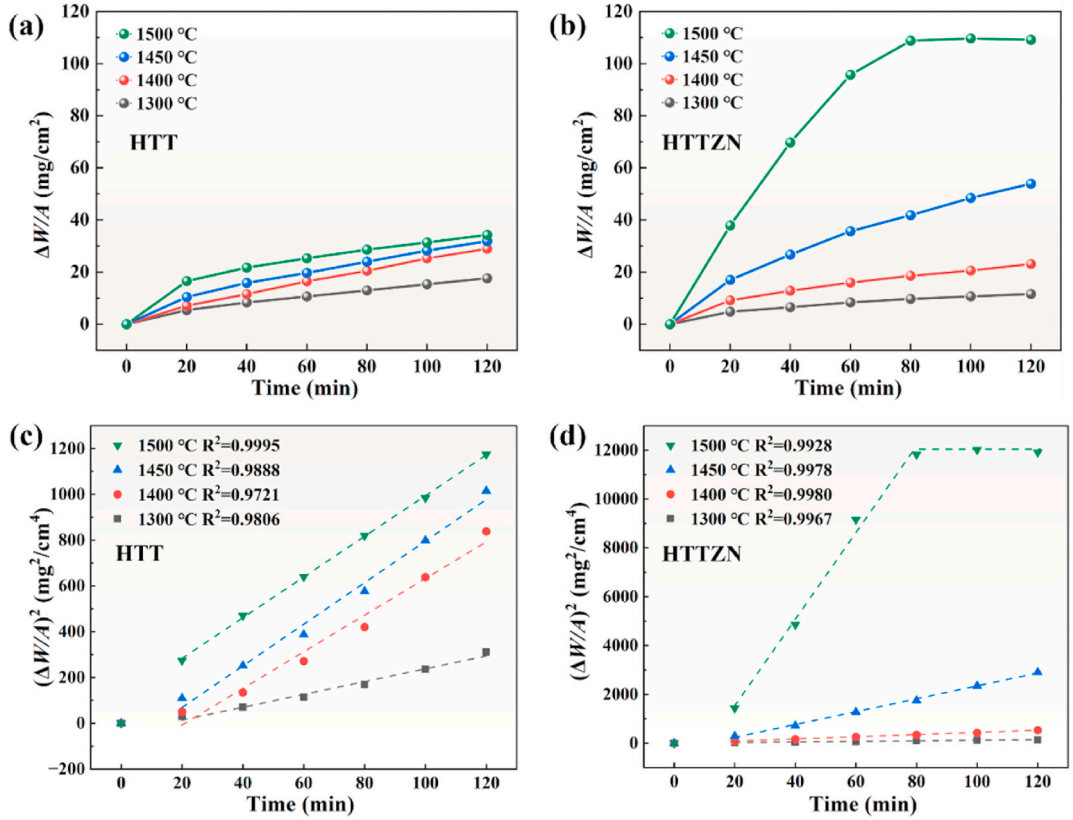

Fig. 5. Mass gain ($\Delta W/A$) as a function of the oxidation time for (a) HTT and (b) HTTZN at 1300–1500 °C; The square of specific mass gain $(\Delta W/A)^2$ as a function of the oxidation time for (c) HTT and (d) HTTZN.

Table 1
The parabolic rate constants and activation energies for HTT and HTTZN.

Specimen	k_p ($mg^2/cm^4 \cdot min$)				Activation energy
	1300 °C	1400 °C	1450 °C	1500 °C	(kJ/mol)
HTT	2.80	8.01	9.09	8.89	185.36
HTTZN	1.14	4.45	26.36	N/A	434.27

previous studies and this work, maintaining stable and excellent oxidation behavior across the temperature range of 1000–1400 °C [26, 30,33,35,43]. In this work, HTTZN showed a rapid increase in mass gain due to the degradation of the oxide layer at temperatures higher than 1450 °C. Compared to other ceramics in Fig. 6, HTT exhibits lower and more stable mass gain at 1300–1500 °C, indicating that the oxide layer on HTT was reliable and protective. Compared with other ceramic systems in Fig. 6, the HTT exhibits significantly lower mass gain within elevated temperature ranges. Notably, its mass gain demonstrates a smooth incremental progression without abrupt increases during thermal elevation, indicating that the surface oxide layer possesses superior oxidation resistance and structural stability.

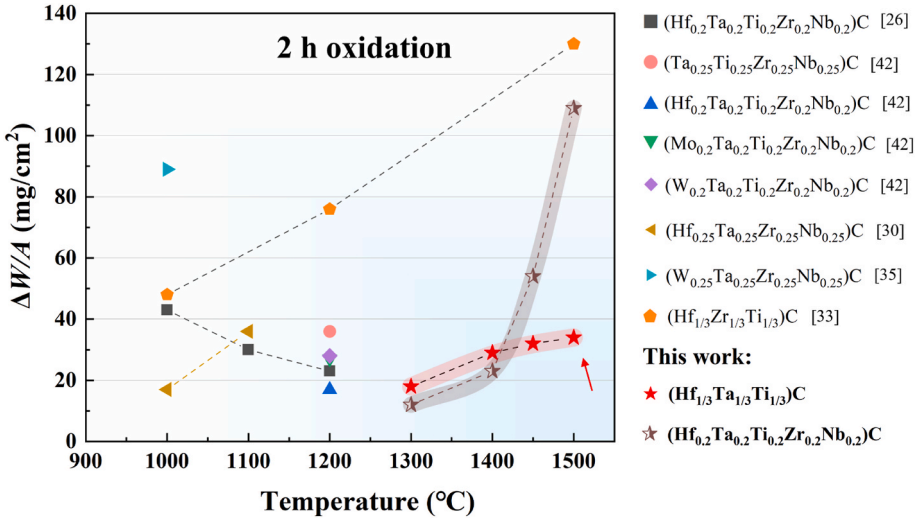

Fig. 6. Oxidation mass gain of the medium and high-entropy carbides at different temperatures for 2 h.

3.4. Microstructure evolution during oxidation

Fig. 7 presents the morphology evolution of HTT and HTTZN specimens after isothermal oxidation. As the oxidation temperature increased from 1300 °C to 1400 °C and then 1450 °C, the grain size of surface oxides on HTT and HTTZN exhibited variation trends of 5.1–6.6-17.2 μm and 5.2-11.8-32.2 μm, respectively. The presence of finer oxide particles within the granular structure of HTT was attributed to the higher melting temperature of these oxides [44]. A dense and irregular oxide layer with a few micro-pores was observed in Fig. 7(a) and (d) on both HTT and HTTZN at 1300 °C. Elevated to 1400 °C, as shown in Fig. 7 (b), more micro-pores were observed along grain boundaries on the surface of HTT. In contrast, the HTTZN surface developed a molten-like oxide layer characterized by reduced surface pores and smoother grain boundaries (Fig. 7(e)). The sintering temperature of a material is conventionally defined as two-thirds of its melting point [45]. The oxides of Nb, Ta, and Ti in HTTZN exhibit significantly lower melting points compared to those of Hf and Zr, as evidenced in Fig. S1. Therefore, the current oxidation temperature of 1400 °C provides the driving force for sintering of these low-melting-point oxides, thereby promoting densification of the oxide layer on HTTZN. For HTT oxidized at 1450 °C, the oxide layer shows a dense structure with near-complete elimination of micro-pores (Fig. 7(c)). Some fine oxide particles were observed, mainly distributed at grain boundaries, which filled the micro-pores in Fig. 7(b). However, the 1450 °C exposure induced multi-scale cracks with dimensional variations on HTTZN, accompanied by the localized emergence of coarse oxide clusters in specific areas of the oxide layer (Fig. 7(f)). The above analyses revealed that the HTT oxide layer maintained superior structural integrity and stability relative to HTTZN in the oxidation tests at 1450 °C.

The elemental distributions in different areas of Fig. 7(c) and (f) are presented in Table 2. The observed Ti enrichment in spot 1, spot 3, and spot 4 can be attributed to its rapid diffusion rate during high-temperature oxidation [25]. Spot 2 on HTT shows a higher content of Ta than that of spot 1, indicating that the newly formed fine oxide particles were Ta-rich oxides. Points 3 and 4 demonstrate comparable element content, and the porous and rough morphology observed in the magnified insert image (Fig. 7(f)) may provide pathways for inward oxygen diffusion, thereby accelerating degradation of the substrate.

The XRD patterns in Fig. 8 show the phase evolution of oxides on HTT and HTTZN from 1300 °C to 1450 °C. Notably, elements within the same periodic group exhibit substitutional behavior, resulting in

Table 2
EDS analyses of different spots in Fig. 6 (at.%).

Spot	Hf	Ta	Zr	Nb	Ti	O
1	7.30	8.67	/	/	29.72	54.31
2	2.10	31.46	/	/	15.90	50.54
3	6.35	4.47	8.26	2.98	14.23	63.71
4	5.46	5.04	6.09	4.23	12.59	66.59

overlapping diffraction peaks of distinct oxides at specific 2θ positions that complicate precise phase identification [39]. The XRD analyses primarily suggest possible phase compositions. As shown in Fig. 8(a), TiO_2 (ICCD card No. 04-027-5652) was detected on the surface of HTT only at 1300 °C, while $HfTiO_4$ (ICCD card No. 00-040-0794), $Hf_6Ta_2O_{17}$ (ICCD card No. 04-025-1940), Ta_2O_5 (ICCD card No. 04-007-0607), and $TiTa_2O_7$ (ICCD card No. 00-021-1424) were detected at both 1300 °C and 1450 °C. The observed formation of complex oxides at 1450 °C, accompanied by diminished TiO_2 diffraction peaks, can be attributed to solid phase reactions among HfO_2, Ta_2O_5, and TiO_2 at elevated temperature [46]. The interaction between these oxidation products is described by reactions (1)–(4):

$$Ta_2O_5(s)+{}_6HfO_2(s)\rightarrow Hf_6Ta_2O_{17}(s) \quad (1)$$

$$TiO_2(s)+HfO_2(s)\rightarrow HfTiO_4(s) \quad (2)$$

$$TiO_2(s)+Ta_2O_5(s)\rightarrow TiTa_2O_7(s) \quad (3)$$

$$TiO_2(s)+Nb_2O_5(s)\rightarrow TiNb_2O_7(s) \quad (4)$$

The identified complex oxide phases exhibited relatively high melting temperatures and possessed dense structures($HfTiO_4$: 1980 °C [47], $TiTa_2O_7$: 1674 °C [48], and $Hf_6Ta_2O_{17}$: 2243 °C [49]). In addition, the diffraction peak of Ta_2O_5 observed at $2\theta = 29.7°$, as indicated by the red arrow in Fig. 8(a), demonstrated a marked decrease in intensity when the oxidation temperature increased from 1300 °C to 1450 °C, indicating a reduced amount of Ta_2O_5 (ICCD card No. 04-007-0607). This is due to the inhibited formation rate of Ta_2O_5 at higher temperatures [31]. For HTTZN, the predominant phase on the surface of the specimen oxidized at 1300 °C was identified as $TiNb_2O_7$ (ICCD card No. 04-007-5182, Fig. 8(b)). As shown in Fig. S4, the PDF cards of $TiNb_2O_7$ and $TiTa_2O_7$ exhibit differences in their characteristic peaks, thereby enabling effective differentiation between these two phases. In addition, the melting point of $TiNb_2O_7$ has not been precisely determined,

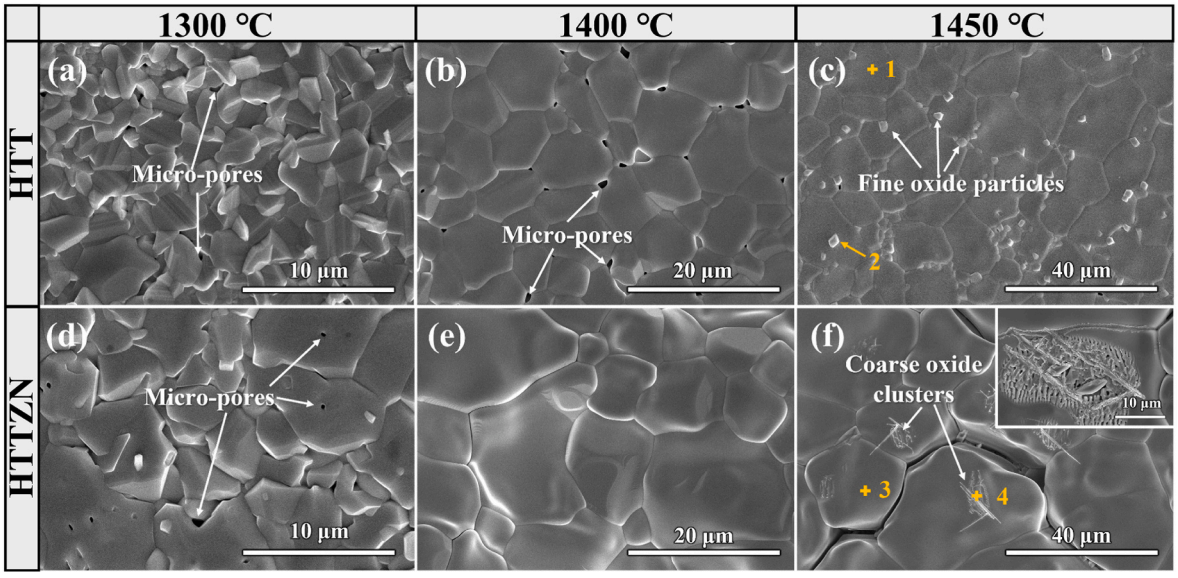

Fig. 7. Surface SEM images of HTT and HTTZN after oxidation for 2 h. (a)–(c) HTT-1300 - 1450 °C; (d)–(f) HTTZN-1300 - 1450 °C.

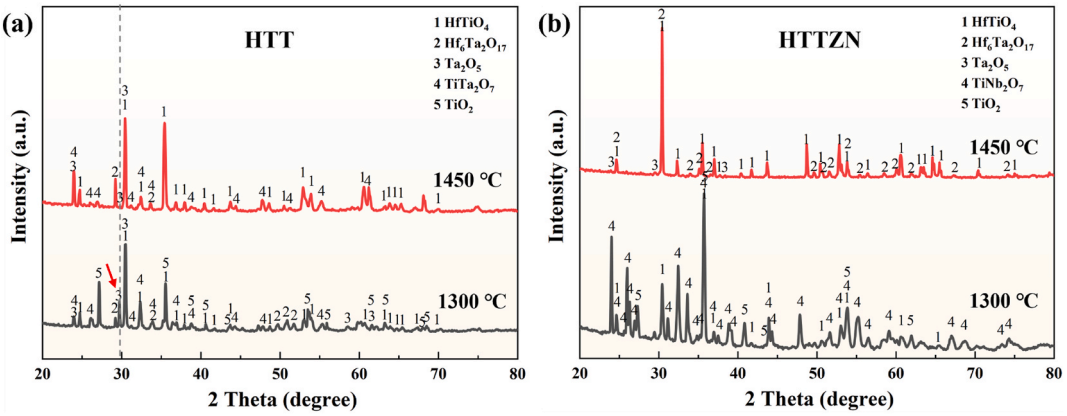

Fig. 8. XRD patterns of (a) HTT and (b) HTTZN after oxidation at 1300 °C and 1450 °C for 2 h.

whereas previous research reported a melting temperature of 1674 °C for $TiTa_2O_7$, suggesting that $TiNb_2O_7$ likely exhibits a lower melting point than 1674 °C [50]. After oxidation at 1450 °C, $TiNb_2O_7$ was no longer detectable, and the oxides on the HTTZN surface were composed of $HfTiO_4$, Ta_2O_5, and $Hf_6Ta_2O_{17}$. These complex oxides have been confirmed to exhibit a dense microstructure, which effectively functions as an oxygen diffusion barrier, thereby substantially improving the oxidation resistance of both HTT and HTTZN [43–45].

Fig. 9 presents the cross-section morphology and corresponding EDS analyses of HTT and HTTZN after 2 h oxidation at 1300 °C. Neither specimen exhibits cracking, large pores, or oxide delamination. It can be observed that the oxide layer of HTT is significantly thicker than that of

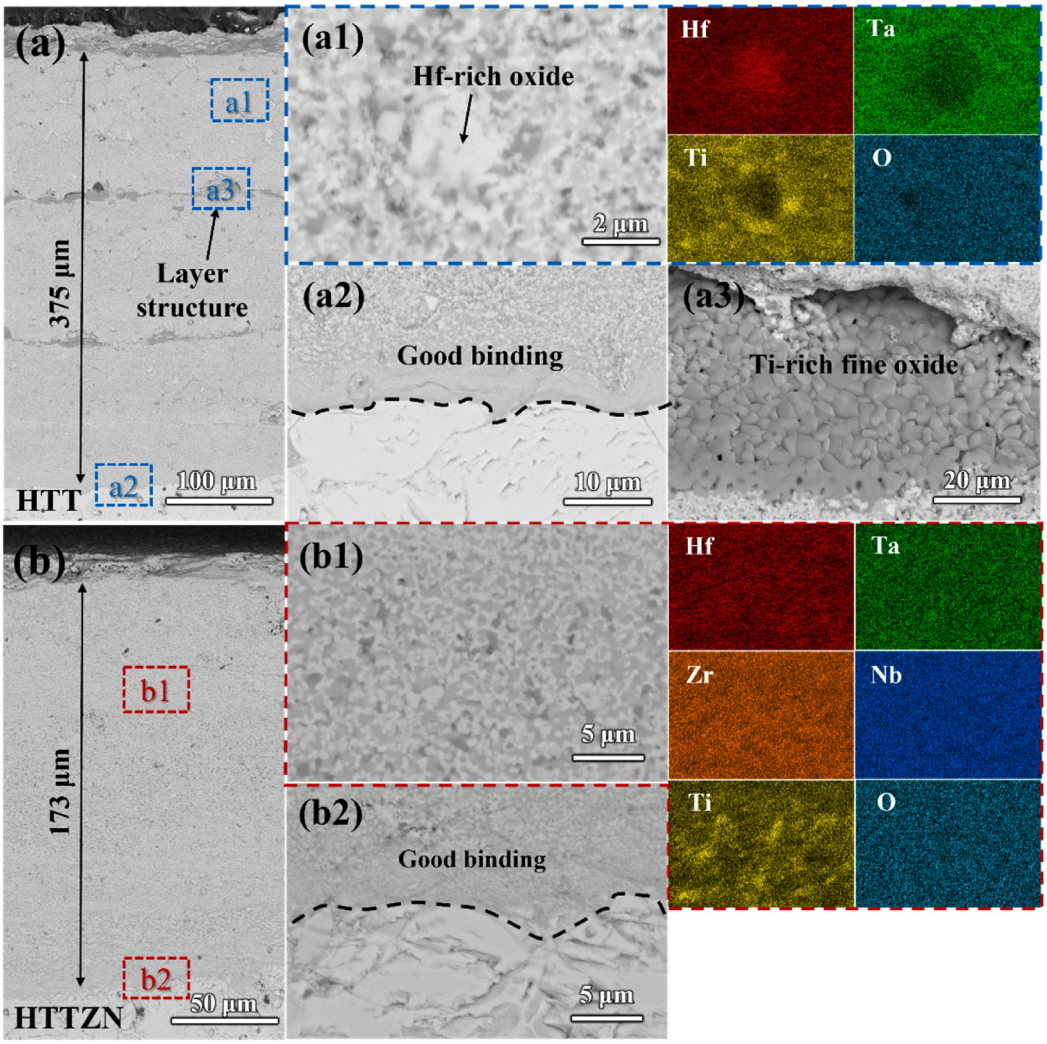

Fig. 9. Cross-section BSE images and EDS results after oxidation at 1300 °C for 2 h. (a) Cross-section morphology of HTT; (a1)-(a3) Magnified images of the corresponding blue square areas in (a) and EDS analysis; (b) Cross-section morphology of HTTZN; (b1)-(b2) Magnified images of the corresponding red square areas in (b) and EDS analysis. (For interpretation of the references to colour in this figure legend, the reader is referred to the Web version of this article.)

HTTZN, which is 375 μm and 173 μm, respectively. Within the cross-section oxide layer of HTT, two dark thin layers were observed in Fig. 8(a), and the enlarged image is shown in Fig. 9(a3), which correspond to the Ti-rich oxide layer according to the EDS result (Hf-4.64 at.%, Ta-5.41 at.%, Ti-26.08 at.%, and O-63.87 at.%). A similar laminated structure was previously reported by Ye et al., which was due to the residual thermal stress during the thermal cycling for weighing [26]. These Ti-rich fine oxides filled the interlayer cracks, which ensured the structural integrity of the whole oxide layer of HTT. The EDS results in Fig. 9(a1) show distinct enrichment of Ti and Hf in the dark and bright areas, respectively. For HTTZN, notable Ti enrichment was observed in the dark areas of the dense oxide layer (Fig. 9(b1)). This alternating bright and dark structure in oxide layers is probably attributed to two critical factors: preferential oxidation at early oxidation stages and disparity in diffusion rates among different elements during subsequent oxidation processes. The interlocking of diverse complex oxides creates a dense layer within the oxide layer, which significantly enhances its oxidation resistance. In addition, as shown in Fig. 9(a2) and (b2), good

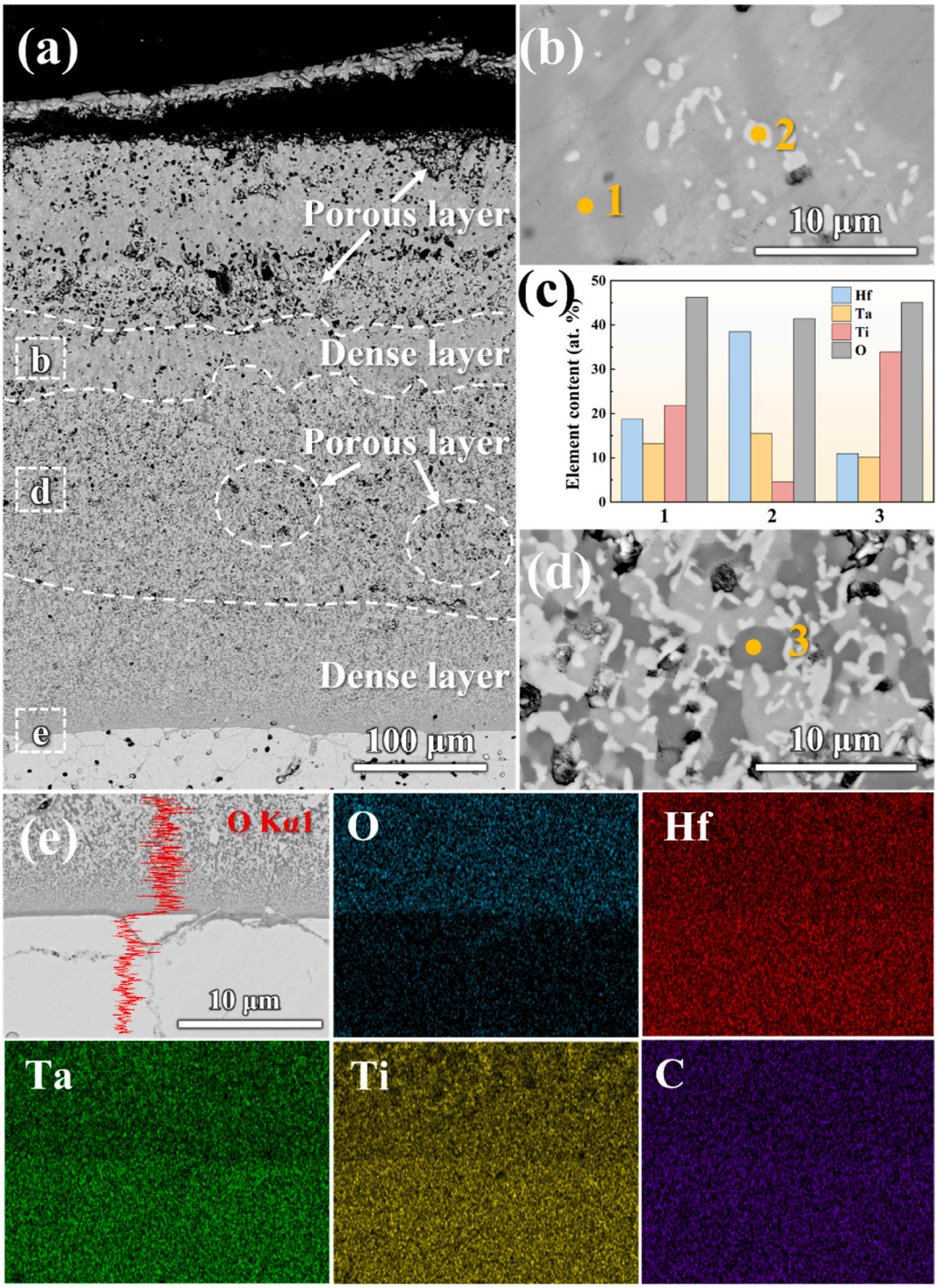

Fig. 10. Cross-section BSE images and EDS results of HTT after oxidation at 1450 °C for 2 h. (a) Cross-section morphology; (b) Dense oxide layer; (c) EDS results of different spots; (d) Porous oxide layer; (e) Interface between the oxide and substrate.

bindings between the substrate and oxide layer were observed in both HTT and HTTZN. The oxide layer structure, thickness, and corresponding oxidation rate k_p discussed above all indicate better oxidation resistance of HTTZN at 1300 °C.

Fig. 10 presents the cross-section morphology and corresponding EDS analyses of HTT after 2 h oxidation at 1450 °C. As shown in Fig. 10 (a), despite minor bulging of the thin outermost oxide layer, the overall oxide layer maintained structural integrity without internal cracks. The average thickness of the surface oxide layer reached 456 μm after 2 h oxidation at 1450 °C, exhibiting a 22 % increase compared to that formed at 1300 °C. In addition, the oxide layer demonstrated an alternating dense and porous structure. The dense layer effectively hindered the inward diffusion of oxygen, while the porous layer provided space for the volume expansion, reducing stress development during temperature cycling [29]. The porous oxide layer formed during the thermal cycling associated with specimen weighing and re-exposure, whereas the dense oxide layer formed during the stable oxidation stage as the specimen reached the target temperature. The enlarged image of the outer dense layer is shown in Fig. 10(b), with the EDS results of spots 1 and 2 summarized in Fig. 10(c). It shows that the outer layer consists primarily of Hf-Ta-Ti-O complex oxides (spot 1) with minor Hf-rich oxide spot 2). The internal dense layer exhibits significant enrichment of Hf-rich oxides, accompanied by the emergence of Ti-rich oxide phases (as identified in spot 3 in Fig. 10(d)). Fig. 10(e) shows the strong binding between the oxide layer and substrate, indicating the approximate thermal expansion coefficient between them. Furthermore, the EDS line scanning and mapping analyses both revealed a sharp decrease in oxygen content upon approaching the substrate area, demonstrating the excellent oxygen barrier performance of the oxide layer. In addition, as shown Fig. S5 and Table S2, the EDS point analysis confirmed that Hf, Ta, and Ti maintained near-equimolar ratios both within the substrate and at the oxide layer/substrate interface, demonstrating preserved entropy stability of the matrix following oxidation.

Fig. 11 presents the cross-section morphology and corresponding EDS analyses of HTTZN after 2 h oxidation at 1450 °C. As shown in Fig. 11(a), extensive pores and large transverse cracks were observed within the oxide layer of HTTZN, resulting in severe delamination. The HTTZN exhibited an average oxide layer thickness of 908 μm, representing a 5.2-fold increase compared to that formed at 1300 °C and doubling the thickness observed on the HTT surface under identical oxidation conditions. The outermost Ti-rich oxide layer enlarged in Fig. 11(b) exhibits a thin and dense microstructure. However, this layer was not continuous enough to be protective, as evidenced by the breakage area. Furthermore, numerous pores were observed beneath the Ti-rich layer, revealing intact Hf-rich oxide particles, which indicates the depletion of low-melting-point oxides during oxidation. The dense oxide layer adjacent to the substrate in Fig. 11(c) was composed of bright (spot 1) and dark (spot 2) phases, which were rich in Hf-Zr and Ti-Ta, respectively. Notably, extensive pores were also observed in the HTTZN substrate after 2 h exposure at 1450 °C, as shown in Fig. 11(d). EDS analysis confirmed high oxygen content in this area (O-22.31 at.%), indicating that the oxide layer failed during the oxidation at 1450 °C, and the substrate has been fully oxidized.

To clarify the effect of thermal cycling on the oxidation behavior, the

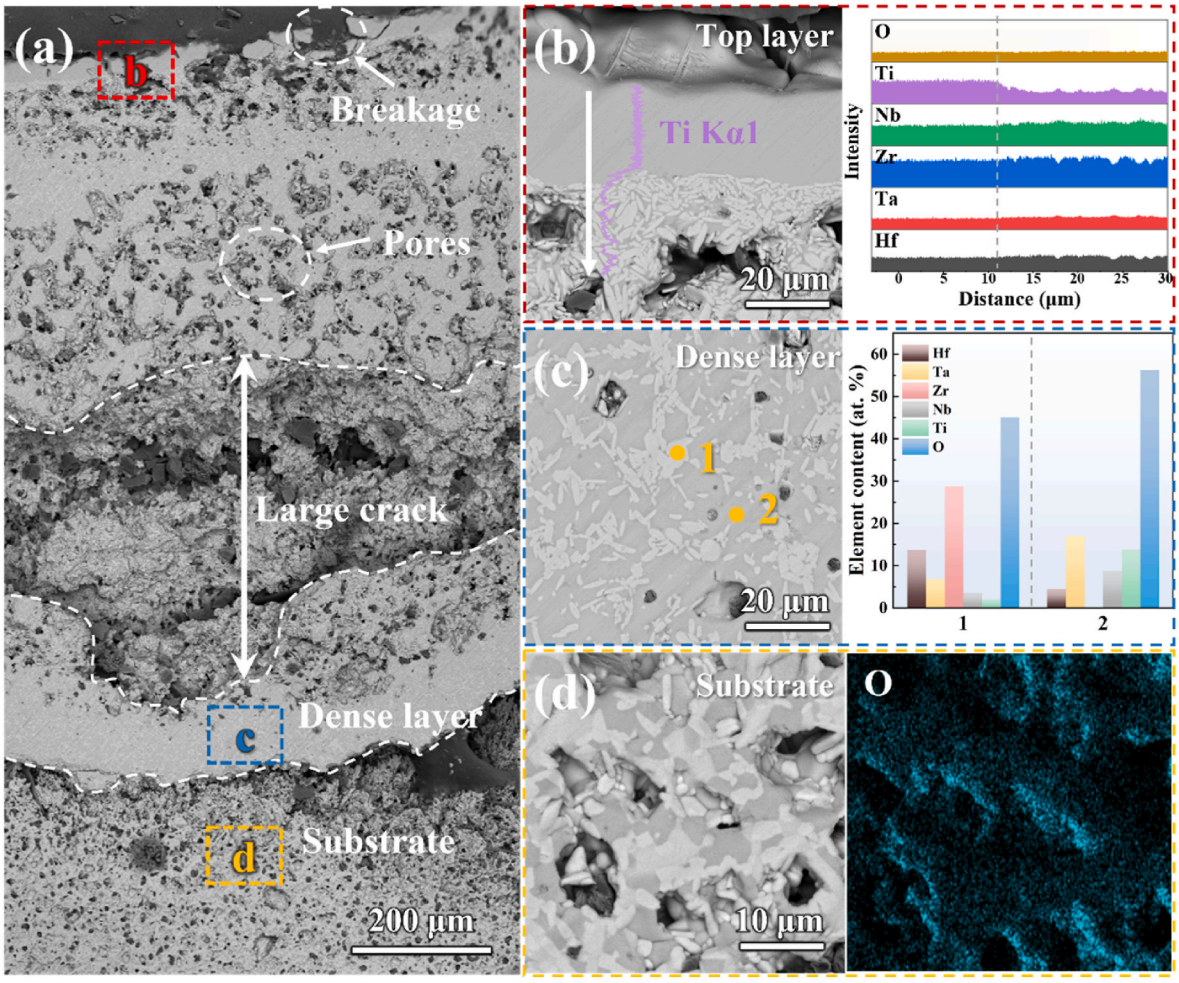

Fig. 11. Cross-section BSE images and EDS results of HTTZN after oxidation at 1450 °C for 2 h. (a) Cross-section morphology; (b) Top oxide layer; (c) Dense oxide layer; (d) Oxidized substrate.

oxidation tests of HTT and HTTZN were conducted at 1450 °C for 2 h without taking out for weighing. The HTT specimen without weighing in Fig. S6(a) exhibits reduced macroscopic cracks compared to those in Fig. 4, while the HTTZN specimen in Fig. S6(b) maintained its original macroscopic morphology with negligible differences. Cross-section BSE images in Fig. S6(c) and (d) reveal that both HTT and HTTZN specimens exhibit fewer pores and cracks compared to those shown in Figs. 10(a) and 11(a). The oxide layer of HTTZN without taking out for weighing remained intact with significantly alleviated delamination compared to Fig. 11(a). These findings indicate that thermal cycling significantly contributes to pore and crack formation in the oxide layer, compromising structural integrity and promoting delamination.

The microstructure analyses of the HTT specimen after oxidation at 1500 °C for 2 h are shown in Fig. 12. According to the Rietveld refinement of the XRD pattern in Fig. 12(a), strong diffraction peaks of the $HfTiO_4$ phase can be detected. The peaks of the remaining oxides were too weak to be accurately identified and refined. As shown in Fig. 12(b) and (c), the oxide on the surface of HTT remained dense and almost crack-free, indicating the outstanding oxidation resistance of the intact structure of the oxide layer. Additionally, the contents of Ti and Hf in the surface oxide of HTT are nearly equivalent, confirming the accuracy of the XRD result. As shown in Fig. 12(d), the cross-section morphology of the oxide layer formed at 1500 °C exhibits a comparable structure to that developed at 1450 °C, and the thickness only increased by 7 %, reaching 488 μm. Due to the excessively high temperature, transverse cracks within the oxide layer formed during oxidation, but the whole oxide layer remained intact without spallation. In addition, the dark areas in Fig. 12(d) are the resin introduced during the specimen embedding. Fig. 12(e) displays the HAADF image and the associated EDS element mapping results for Hf, Ta, Ti, and O of the oxide particle specimen. The Ti exhibited lower content in the blue square area and higher content in the yellow square area of the oxide particle, while corresponding SAED analyses identified these two distinct areas as the monoclinic Ta_2O_5 and orthorhombic $HfTiO_4$, respectively. As the primary phase in the oxide, $HfTiO_4$ demonstrated the capability to form and sinter into a dense and continuous oxide layer at elevated temperatures up to 1500 °C [51].

3.5. Oxidation mechanism

Fig. 13 shows the Ellingham diagram for the metal-oxide reactions, which is a useful predictive tool in comparing the relative thermodynamic stabilities of the oxides that form in a multicomponent system [36]. The lower line in the plot indicates the oxide has a lower ΔG, which is more thermodynamically stable. When exposed to a sufficiently oxidizing environment, all species in contact with the environment will oxidize. However, due to the preferential oxidation, different elements exhibit sequential oxidation priorities, which implies varied consumption rates of the constituent metallic elements. Differential depletion of constituent elements within the substrate can induce instability in the substrate, triggering the development of other phases. Such

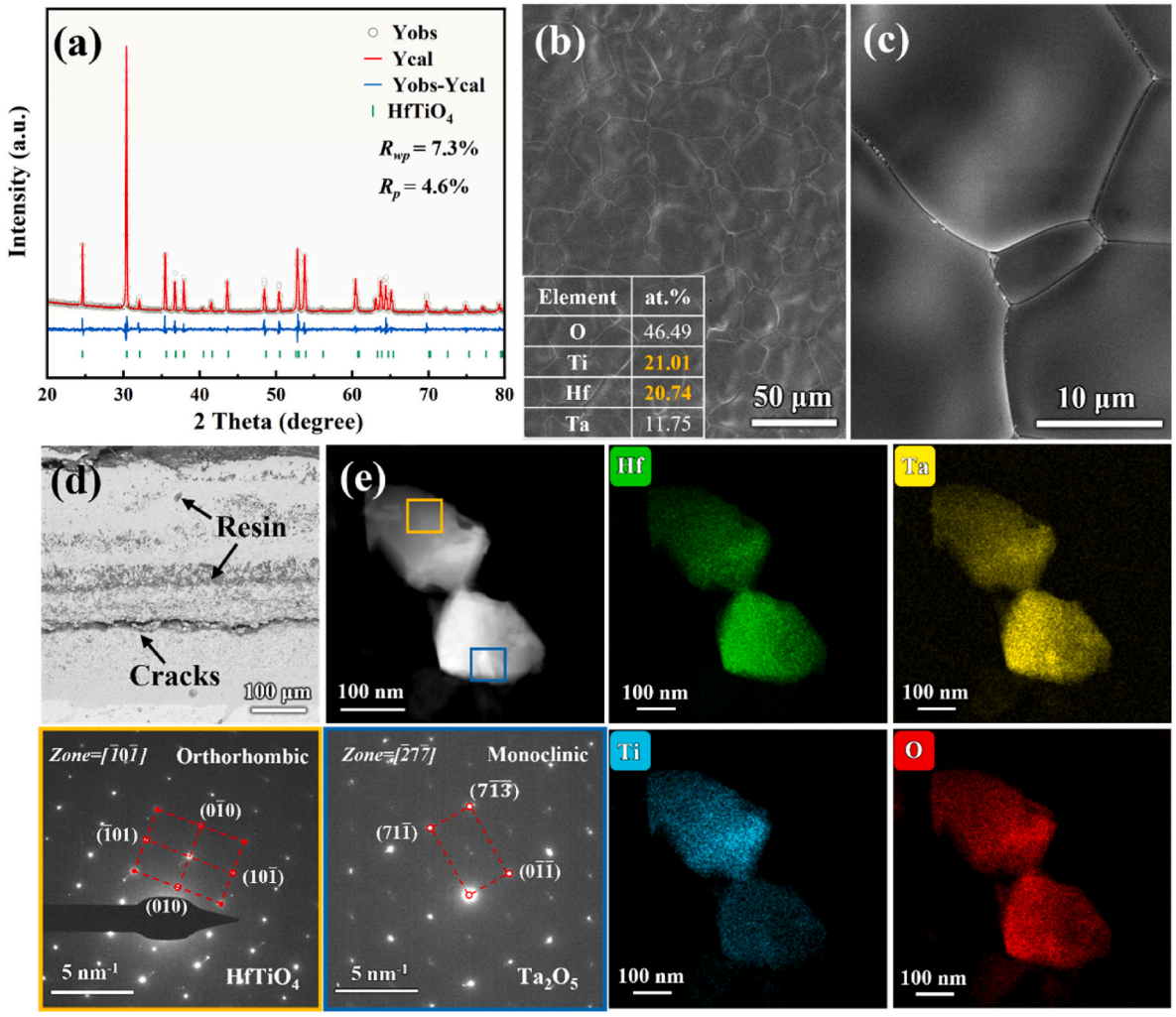

Fig. 12. Phase and structure analyses of HTT after oxidation at 1500 °C for 2 h. (a) The Rietveld patterns; (b) Surface SEM image; (c) Magnified surface SEM image; (d) Cross-section morphology; (e) TEM, EDS, and SAED analyses of surface oxide.

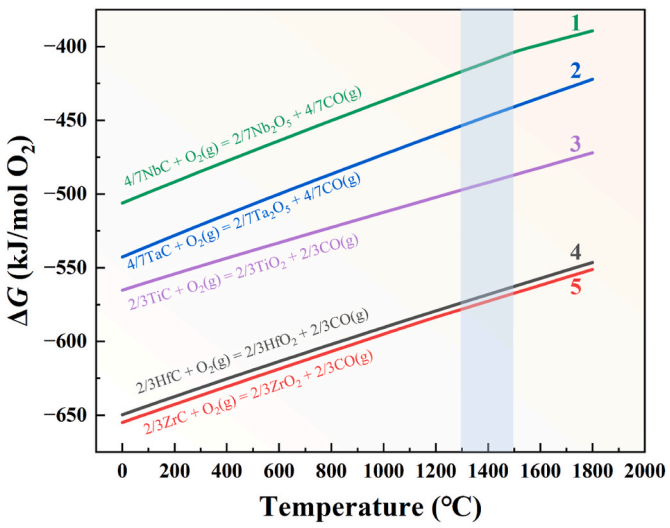

Fig. 13. Ellingham diagram of the transition elements in HTT and HTTZN.

microstructural evolution could counteract the anticipated performance benefits derived from the high entropy design strategy [39]. When designing the HTT system, we strategically introduced TiC into the HfC-TaC, due to its oxide's thermodynamic stability being close to HfC and TaC (Fig. 13 lines 2, 3, and 4). The diminished preferential oxidation sequence of Hf, Ta, and Ti elements reduces the discrepancy in their depletion rates within the HTT substrate, which consequently enhances the stability of HTT's elevated temperature properties. During oxidation at 1300–1500 °C, the dense and continuous oxide layer showed superior oxidation resistance, demonstrating its significant potential for high-temperature applications.

Fig. 14 illustrates the oxidation mechanism of HTT and HTTZN at different temperatures. At 1300 °C, the melting points of constituent metal oxides exceed the oxidation temperature, and both specimens developed dense oxide layers. HTT presents a thicker oxide layer at 1300 °C, and the fine Ti-rich oxide played a critical role in sealing cracks and maintaining the intact structure of the oxide layer. For HTT oxidized at 1450 °C, the appropriate PBR value of oxides and the well-matched coefficient of thermal expansion between the oxide layer and the substrate synergistically maintain a dense and stable oxide layer structure. The layered structure of the oxide provides dual protective mechanisms: the dense layers effectively retard inward diffusion of oxygen, while the intervening porous layers accommodate thermal stress generated during oxidation. For HTTZN, the high configurational entropy contributes to the sluggish diffusion effect, effectively suppressing inward diffusion of oxygen. The synergistic effect of multi-principal elements enabled HTTZN to form a dense oxide layer during oxidation. However, as the oxidation temperature increased to 1450 °C, the low-melting-point oxides in HTTZN were prone to melt and volatilize, while the phase transformation of ZrO_2 introduces substantial stresses within the oxide layer, leading to severe cracking and spallation. At higher temperatures (1450 °C and 1500 °C), the entropy-stabilization benefits were partially negated by deleterious high-temperature behavior of specific constituents, demonstrating the temperature-dependent effectiveness of high-entropy design strategies.

4. Conclusion

This work compared the oxidation behavior of medium-entropy carbide HTZ, HTN, HTT, and high-entropy carbide HTTZN, and the underlying mechanism was discussed. The formation of oxides by Zr and Nb during thermal cycling degraded the integrity of the oxide layer,

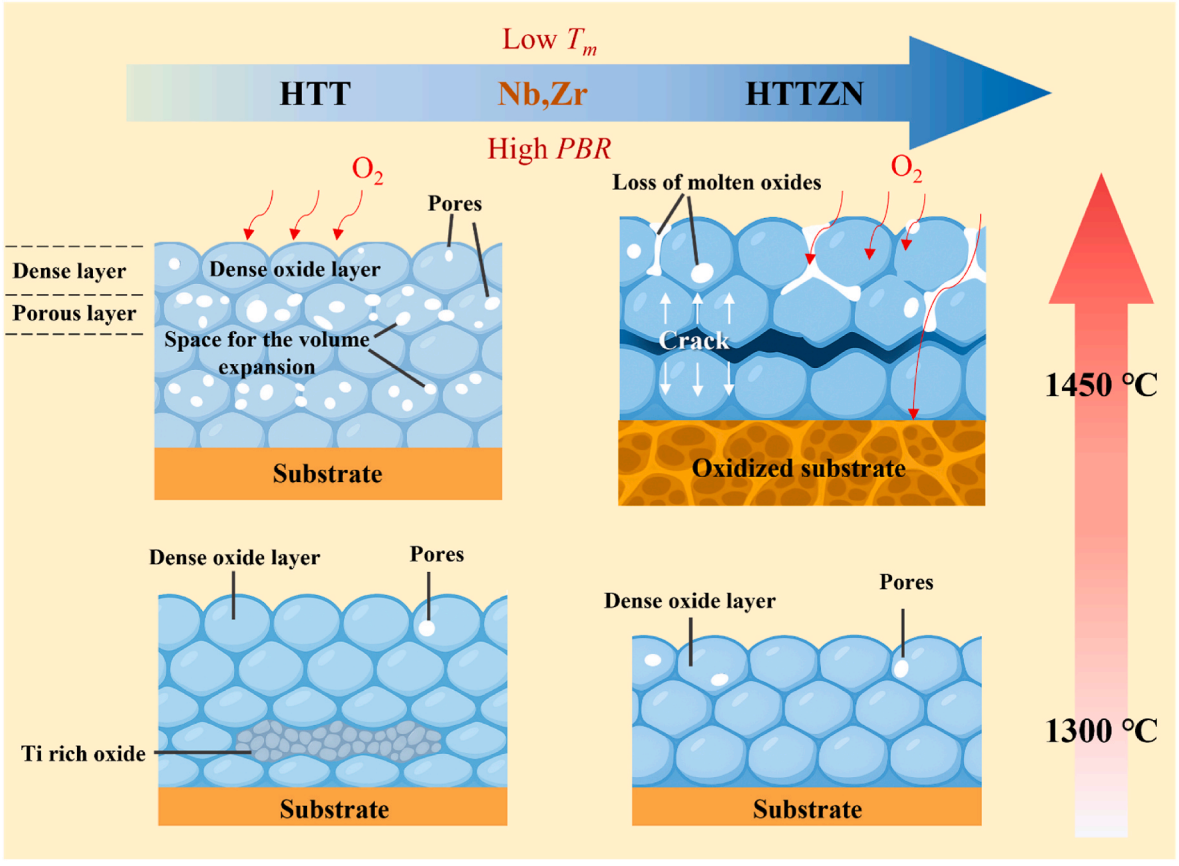

Fig. 14. Schematic structure of HTT and HTTZN oxidized at different temperatures.

thereby resulting in substrate failure of HTZ and HTN. At 1300 °C and 1400 °C, the sluggish diffusion effect and synergistic effect of multi-principal elements enabled HTTZN to form a dense and thin oxide layer. Above 1450 °C, the excessive thermal stress within the oxide layer and the loss of low-melting-point oxides lead to catastrophic failure of the surface oxide layer, resulting in complete oxidation of the HTTZN substrate. From 1300 °C to 1500 °C, a dense and stable oxide layer formed on HTT, effectively hindering the inward diffusion of oxygen. The alternating dense/porous layered structure of the oxide layer at 1450 °C alleviated thermal stress. The preferential oxidation of Ti and Hf at 1500 °C induced the formation of $HfTiO_4$, which contributed to exceptional oxidation resistance with remarkable stability. This work elucidates the temperature-dependent interplay between entropy and composition, thereby providing foundational insights for tailoring UHTCs across distinct temperature regimes.

CRediT authorship contribution statement

Guoming Yi: Writing – original draft, Methodology, Investigation, Data curation, Conceptualization. **Juan Kuang:** Investigation, Conceptualization. **Gaopeng Zou:** Investigation, Conceptualization. **Bo Sun:** Methodology, Investigation. **Huanyu Mo:** Data curation. **Qianqian Wang:** Writing – review & editing, Supervision, Project administration, Funding acquisition, Conceptualization. **Baolong Shen:** Supervision, Project administration, Funding acquisition, Conceptualization.

Declaration of competing interest

The authors declare that they have no known competing financial interests or personal relationships that could have appeared to influence the work reported in this paper.

Acknowledgments

This work is supported by the National Natural Science Foundation of China (52231005, 52571183), the Jiangsu Provincial Key Research and Development Program (BE2021088), Opening Project of Jiangsu Key Laboratory for Advanced Metallic Materials (AMM2020A01, AMM2024A02, AMM2023B05), and Jiangsu Key Laboratory of Advanced Structural Materials and Application Technology (ASMA202302).

Appendix A. Supplementary data

Supplementary data to this article can be found online at https://doi.org/10.1016/j.ceramint.2026.01.115.

Data availability

Data will be made available on request.

References

[1] R. Savino, M. De Stefano Fumo, D. Paterna, M. Serpico, Aerothermodynamic study of UHTC-based thermal protection systems, Aerosp. Sci. Technol. 9 (2005) 151–160, https://doi.org/10.1016/j.ast.2004.12.003.

[2] M. Le-Huu, H. Schmitt, S. Noll, M. Grieb, F.F. Schrey, A.J. Bauer, L. Frey, H. Ryssel, Investigation of the reliability of 4H–SiC MOS devices for high temperature applications, Microelectron. Reliab. 51 (2011) 1346–1350, https://doi.org/10.1016/j.microrel.2011.03.015.

[3] Y. Katoh, L.L. Snead, I. Szlufarska, W.J. Weber, Radiation effects in SiC for nuclear structural applications, Curr. Opin. Solid State Mater. Sci. 16 (2012) 143–152, https://doi.org/10.1016/j.cossms.2012.03.005.

[4] K. Yueh, K.A. Terrani, Silicon carbide composite for light water reactor fuel assembly applications, J. Nucl. Mater. 448 (2014) 380–388, https://doi.org/10.1016/j.jnucmat.2013.12.004.

[5] J. Li, Y. Zhang, Y. Zhao, Y. Zou, J. Lv, J. Li, A novel $(Hf_{1/3}Zr_{1/3}Ti_{1/3})C$ medium-entropy carbide coating with excellent long-life ablation resistance applied above 2100 °C, Compos. Pt. B-Eng. 251 (2023), https://doi.org/10.1016/j.compositesb.2022.110467.

[6] B. Zhang, J. Yin, J. Chen, Y. Huang, X. Liu, Z. Huang, Pressureless densification, microstructure tailoring and properties of $Ta_{0.8}Hf_{0.2}C$-based composites, J. Eur. Ceram. Soc. 38 (2018) 1227–1236, https://doi.org/10.1016/j.jeurceramsoc.2017.10.025.

[7] H. Chen, H. Xiang, F.-Z. Dai, J. Liu, Y. Lei, J. Zhang, Y. Zhou, High porosity and low thermal conductivity high entropy $(Zr_{0.2}Hf_{0.2}Ti_{0.2}Nb_{0.2}Ta_{0.2})C$, J. Mater. Sci. Technol. 35 (2019) 1700–1705, https://doi.org/10.1016/j.jmst.2019.04.006.

[8] X. Yan, L. Constantin, Y. Lu, J.-F. Silvain, M. Nastasi, B. Cui, $(Hf_{0.2}Zr_{0.2}Ta_{0.2}Nb_{0.2}Ti_{0.2})C$ high-entropy ceramics with low thermal conductivity, J. Am. Ceram. Soc. 101 (2018) 4486–4491, https://doi.org/10.1111/jace.15779.

[9] E. Castle, T. Csanádi, S. Grasso, J. Dusza, M. Reece, Processing and properties of high-entropy ultra-high temperature carbides, Sci. Rep. 8 (2018), https://doi.org/10.1038/s41598-018-26827-1.

[10] W. Zhang, L. Chen, C. Xu, W. Lu, Y. Wang, J. Ouyang, Y. Zhou, Densification, microstructure and mechanical properties of multicomponent (TiZrHfNbTaMo)C ceramic prepared by pressureless sintering, J. Mater. Sci. Technol. 72 (2021) 23–28, https://doi.org/10.1016/j.jmst.2020.07.019.

[11] O. Cedillos-Barraza, D. Manara, K. Boboridis, T. Watkins, S. Grasso, D. D. Jayaseelan, R.J.M. Konings, M.J. Reece, W.E. Lee, Investigating the highest melting temperature materials: a laser melting study of the TaC-HfC system, Sci. Rep. 6 (2016) 37962, https://doi.org/10.1038/srep37962.

[12] J. Binner, M. Porter, B. Baker, J. Zou, V. Venkatachalam, V.R. Diaz, A. D'Angio, P. Ramanujam, T. Zhang, T.S.R.C. Murthy, Selection, processing, properties and applications of ultra-high temperature ceramic matrix composites, UHTCMCs – a review, Int. Mater. Rev. 65 (2020) 389–444, https://doi.org/10.1080/09506608.2019.1652006.

[13] W.G. Fahrenholtz, G.E. Hilmas, Ultra-high temperature ceramics: materials for extreme environments, Scr. Mater. 129 (2017) 94–99, https://doi.org/10.1016/j.scriptamat.2016.10.018.

[14] S.T. Oyama, Introduction to the chemistry of transition metal carbides and nitrides, in: S.T. Oyama (Ed.), The Chemistry of Transition Metal Carbides and Nitrides, Springer Netherlands, Dordrecht, 1996, pp. 1–27, https://doi.org/10.1007/978-94-009-1565-7_1.

[15] T.J. Harrington, J. Gild, P. Sarker, C. Toher, C.M. Rost, O.F. Dippo, C. McElfresh, K. Kaufmann, E. Marin, L. Borowski, P. Hopkins, J. Luo, S. Curtarolo, D. Brenner, K. Vecchio, Phase stability and mechanical properties of novel high entropy transition metal carbides, Acta Mater. 166 (2019) 271–280, https://doi.org/10.1016/J.ACTAMAT.2018.12.054.

[16] B. Ye, T. Wen, M.C. Nguyen, L. Hao, C.-Z. Wang, Y. Chu, First-principles study, fabrication and characterization of $(Zr_{0.25}Nb_{0.25}Ti_{0.25}V_{0.25})C$ high-entropy ceramics, Acta Mater. 170 (2019) 15–23, https://doi.org/10.1016/j.actamat.2019.03.021.

[17] J. Dusza, P. Švec, V. Girman, R. Sedlák, E.G. Castle, T. Csanádi, A. Kovalčíková, M. J. Reece, Microstructure of (Hf-Ta-Zr-Nb)C high-entropy carbide at micro and nano/atomic level, J. Eur. Ceram. Soc. 38 (2018) 4303–4307, https://doi.org/10.1016/j.jeurceramsoc.2018.05.006.

[18] J. Gild, Y. Zhang, T. Harrington, S. Jiang, T. Hu, M. Quinn, W.M. Mellor, N. Zhou, K. Vecchio, J. Luo, High-entropy metal diborides: a new class of high-entropy materials and a new type of ultrahigh temperature ceramics, Sci. Rep. 6 (2016) 37946, doi:10.1038/srep37946.

[19] Y. Li, L. He, H. Pan, S. Zhao, Z. Wu, Compositional optimization for enhanced oxidation resistance of high-entropy carbide ceramics, Acta Mater. 282 (2025) 120463, https://doi.org/10.1016/j.actamat.2024.120463.

[20] J. Zhang, S. Wang, W. Li, Y. Yu, J. Jiang, Understanding the oxidation behavior of Ta–Hf–C ternary ceramics at high temperature, Corros. Sci. 164 (2020) 108348, https://doi.org/10.1016/j.corsci.2019.108348.

[21] D.-L. Yung, B. Maaten, M. Antonov, I. Hussainova, Oxidation of spark plasma sintered ZrC-mo and ZrC-TiC composites, Int. J. Refract. Met. Hard Mater. 66 (2017) 244–251, https://doi.org/10.1016/j.ijrmhm.2017.03.019.

[22] S. Chen, Z. Chen, J. Wang, Y. Zeng, W. Song, X. Xiong, X. Li, T. Li, Y. Wang, Insight into the effect of Ti substitutions on the static oxidation behavior of (Hf, Ti)C at 2500 °C, Adv. Powder Mater. 3 (2024) 100168, https://doi.org/10.1016/j.apmate.2023.100168.

[23] F. Müller, B. Gorr, H.-J. Christ, J. Müller, B. Butz, H. Chen, A. Kauffmann, M. Heilmaier, On the oxidation mechanism of refractory high entropy alloys, Corros. Sci. 159 (2019) 108161, https://doi.org/10.1016/j.corsci.2019.108161.

[24] T.M. Butler, K.J. Chaput, J.R. Dietrich, O.N. Senkov, High temperature oxidation behaviors of equimolar NbTiZrV and NbTiZrCr refractory complex concentrated alloys (RCCAs), J. Alloys Compd. 729 (2017) 1004–1019, https://doi.org/10.1016/j.jallcom.2017.09.164.

[25] H. Wang, X. Han, W. Liu, Y. Wang, Oxidation behavior of high-entropy carbide $(Hf_{0.2}Ta_{0.2}Zr_{0.2}Ti_{0.2}Nb_{0.2})C$ at 1400-1600 °C, Ceram. Int. 47 (2021) 10848–10854, https://doi.org/10.1016/j.ceramint.2020.12.201.

[26] B. Ye, T. Wen, D. Liu, Y. Chu, Oxidation behavior of $(Hf_{0.2}Zr_{0.2}Ta_{0.2}Nb_{0.2}Ti_{0.2})C$ high-entropy ceramics at 1073-1473 K in air, Corros. Sci. 153 (2019) 327–332, https://doi.org/10.1016/j.corsci.2019.04.001.

[27] J. Zhou, J. Zhang, F. Zhang, B. Niu, L. Lei, W. Wang, High-entropy carbide: a novel class of multicomponent ceramics, Ceram. Int. 44 (2018) 22014–22018, https://doi.org/10.1016/j.ceramint.2018.08.100.

[28] B. Ye, T. Wen, Y. Chu, High-temperature oxidation behavior of $(Hf_{0.2}Zr_{0.2}Ta_{0.2}Nb_{0.2}Ti_{0.2})C$ high-entropy ceramics in air, J. Am. Ceram. Soc. 103 (2020) 500–507, https://doi.org/10.1111/jace.16725.

[29] Y. Wang, M.J. Reece, Oxidation resistance of (Hf-Ta-Zr-Nb)C high entropy carbide powders compared with the component monocarbides and binary carbide powders, Scr. Mater. 193 (2021) 86–90, https://doi.org/10.1016/j.scriptamat.2020.10.038.

[30] Y. Wang, R. Zhang, B. Zhang, O. Skurikhina, P. Balaz, V. Araullo-Peters, M. J. Reece, The role of multi-elements and interlayer on the oxidation behaviour of (Hf-Ta-Zr-Nb)C high entropy ceramics, Corros. Sci. 176 (2020) 109019, https://doi.org/10.1016/j.corsci.2020.109019.

[31] H. Wang, S. Wang, Y. Cao, W. Liu, Y. Wang, Oxidation behaviors of $(Hf_{0.25}Zr_{0.25}Ta_{0.25}Nb_{0.25})C$ and $(Hf_{0.25}Zr_{0.25}Ta_{0.25}Nb_{0.25})C$-SiC at 1300-1500 °C, J. Mater. Sci. Technol. 60 (2021) 147–155, https://doi.org/10.1016/j.jmst.2020.05.037.

[32] H. Lun, Y. Zeng, X. Xiong, Z. Ye, Z. Zhang, X. Li, H. Chen, Y. Liu, Oxidation behavior of non-stoichiometric (Zr,Hf,Ti)Cx carbide solid solution powders in air, J. Adv. Ceram. 10 (2021) 741–757, https://doi.org/10.1007/s40145-021-0469-y.

[33] F. Xie, J. Yin, X. Xiong, Z. Chen, S. Chen, W. Song, H. Zhang, J. Zuo, B. Yang, High-temperature oxidation and ablation behavior of $(Zr_{1/3}Hf_{1/3}Ti_{1/3})C$ ceramic, J. Eur. Ceram. Soc. 44 (2024) 116784, https://doi.org/10.1016/j.jeurceramsoc.2024.116784.

[34] S. Chen, J. Wang, Z. Chen, W. Song, Y. Zeng, X. Li, T. Li, X. Xiong, Nb- and Ta-doped (Hf,Zr,Ti)C multicomponent carbides with enhanced oxidation resistance at 2500 °C, J. Adv. Ceram. 13 (2024) 332–344, https://doi.org/10.26599/JAC.2024.9220856.

[35] H. Chen, L. Wang, L. He, Z. Li, H. Yan, T. Yang, Y. Ma, F. Peng, Z. Wu, Oxidation behavior of (NbTaZrW)C high-entropy carbide at 800-1000 °C, Mater. Char. 189 (2022) 111932, https://doi.org/10.1016/j.matchar.2022.111932.

[36] L. Backman, E.J. Opila, Thermodynamic assessment of the group IV, V and VI oxides for the design of oxidation resistant multi-principal component materials, J. Eur. Ceram. Soc. 39 (2019) 1796–1802, https://doi.org/10.1016/j.jeurceramsoc.2018.11.004.

[37] C. Huo, L. Guo, C. Wang, L. Zhou, J. Wang, K. Li, Microstructure and high temperature anti-ablation behavior of Cr-modified ZrC coating for SiC-coated carbon/carbon composites, Ceram. Int. 45 (2019) 1777–1789, https://doi.org/10.1016/j.ceramint.2018.10.063.

[38] M. Rühle, Microscopy of structural ceramics, Adv. Mater. 9 (1997) 195–217, https://doi.org/10.1002/adma.19970090304.

[39] L. Backman, J. Gild, J. Luo, E.J. Opila, Part II: experimental verification of computationally predicted preferential oxidation of refractory high entropy ultra-high temperature ceramics, Acta Mater. 197 (2020) 81–90, https://doi.org/10.1016/j.actamat.2020.07.004.

[40] L. Zheng, X. Luo, C. Fang, C. Zeng, X. Zhang, Z. Zhang, M. Zhang, Q. Huang, Ablation behaviour and mechanism of Mg-modified ZrC-SiC composite in plasma ablation flame, Corros. Sci. 206 (2022) 110523, https://doi.org/10.1016/j.corsci.2022.110523.

[41] B.E. Deal, A.S. Grove, General relationship for the thermal oxidation of silicon, J. Appl. Phys. 36 (1965) 3770–3778, https://doi.org/10.1063/1.1713945.

[42] Y. Tan, C. Chen, S. Li, X. Han, J. Xue, T. Liu, X. Zhou, H. Zhang, Oxidation behaviours of high-entropy transition metal carbides in 1200 °C water vapor, J. Alloys Compd. 816 (2020) 152523, https://doi.org/10.1016/j.jallcom.2019.152523.

[43] S. Yudin, A. Sedegov, D. Moskovskikh, S. Volodko, K. Kuskov, V. Suvorova, S. Danilova-Tretiak, S. Vorotilo, A. Nepapushev, A. Khort, Mechanism and kinetics of high-temperature oxidation of medium- and high-entropy carbides in air, Mater. Des. 231 (2023) 112048, https://doi.org/10.1016/j.matdes.2023.112048.

[44] A. Nisar, T. Dolmetsch, T. Paul, T.S. Sakthivel, C. Zhang, B. Boesl, S. Seal, A. Agarwal, Unveiling enhanced oxidation resistance and mechanical integrity of multicomponent ultra-high temperature carbides, J. Am. Ceram. Soc. 105 (2022) 2500–2516, https://doi.org/10.1111/jace.18281.

[45] C. Zhang, B. Boesl, A. Agarwal, Oxidation resistance of tantalum carbide-hafnium carbide solid solutions under the extreme conditions of a plasma jet, Ceram. Int. 43 (2017) 14798–14806, https://doi.org/10.1016/j.ceramint.2017.07.227.

[46] S. He, Y. Liu, Z. Ma, S. Zhu, L. Liu, G. Mu, Y. Li, Study on anti-ablation properties of HfB_2-$TaSi_2$ coatings prepared by atmospheric plasma spraying, J. Alloys Compd. 999 (2024) 175069, https://doi.org/10.1016/j.jallcom.2024.175069.

[47] J.P. Coutures, J. Coutures, The system HfO_2-TiO_2, J. Am. Ceram. Soc. 70 (1987) 383–387, https://doi.org/10.1111/j.1151-2916.1987.tb05655.x.

[48] J.L. Waring, R.S. Roth, Effect of oxide additions on polymorphism of tantalum pentoxide (system Ta_2O_5-TiO_2), J. Res. Natl. Bur. Stand., Sect. A 72A (1968) 175, https://doi.org/10.6028/jres.072A.018.

[49] S.J. McCormack, K.-P. Tseng, R.J.K. Weber, D. Kapush, S.V. Ushakov, A. Navrotsky, W.M. Kriven, In-situ determination of the HfO_2–Ta_2O_5-temperature phase diagram up to 3000 °C, J. Am. Ceram. Soc. 102 (2019) 4848–4861, https://doi.org/10.1111/jace.16271.

[50] J.L. Waring, R.S. Roth, Effect of oxide additions on polymorphism of tantalum pentoxide (system Ta_2O_5-TiO_2), J. Res. Natl. Bur. Stand., Sect. A 72A (1968) 175, https://doi.org/10.6028/jres.072a.018.

[51] L. Lu, T. Wen, W. Li, Q. Wen, Z. Yu, S. Tao, J. Yang, Y. Wang, X. Luan, X. Xiong, R. Riedel, Single-source-precursor synthesis of dense monolithic SiC/$(Ti_{0.25}Zr_{0.25}Hf_{0.25}Ta_{0.25})C$ ceramic nanocomposite with excellent high-temperature oxidation resistance, J. Eur. Ceram. Soc. 44 (2024) 595–609, https://doi.org/10.1016/j.jeurceramsoc.2023.09.074.